Geosci. Model Dev. Discuss., 2, 845–887, 2009
www.geosci-model-dev-discuss.net/2/845/2009/

Geoscientific
Model Development
Discussions

Geoscientific Model Development Discussions is the access reviewed discussion forum of *Geoscientific Model Development*

Bergen earth system model (BCM-C): model description and regional climate-carbon cycle feedbacks assessment

J. F. Tjiputra[1,2], K. Assmann[1,2], M. Bentsen[2,3], I. Bethke[2,3], O. H. Otterå[2,3], C. Sturm[4], and C. Heinze[1,2]

[1]University of Bergen, Department of Geophysics, Allégaten 70, 5007 Bergen, Norway
[2]Bjerknes Centre for Climate Research, Allégaten 55, 5007 Bergen, Norway
[3]Nansen Environmental and Remote Sensing Center, Thormølensgate 47, 5006 Bergen, Norway
[4]Bert Bolin Centre for Climate Research, Svante Arrhenius väg 8 C, 106 91 Stockholm, Sweden

Received: 12 May 2009 – Accepted: 30 Jun 2009 – Published: 8 July 2009

Correspondence to: J. F. Tjiputra (jerry.tjiputra@bjerknes.uib.no)

Published by Copernicus Publications on behalf of the European Geosciences Union.

Abstract

A complex earth system model is developed by coupling terrestrial and oceanic carbon cycle models into the Bergen Climate Model. Two model simulations (one with climate change inclusions and the other without) are generated to study the large scale climate and carbon cycle variability as well as its feedback for the period 1850–2100. The simulations are performed based on historical and future IPCC CO_2 emission scenarios. Globally, a pronounced positive climate-carbon cycle feedback is simulated by the terrestrial carbon cycle model, but less significant signals are shown by the oceanic counterpart. Over land, the regional climate-carbon cycle feedback is highlighted by increased soil respiration, which exceeds the enhanced production due to the atmospheric CO_2 fertilization effect, in the equatorial and northern hemisphere mid-latitude regions. Although the model generates nearly identical global oceanic carbon uptake between the coupled and uncoupled simulations, our analysis indicates that there are substantial temporal and spatial variations in air-sea CO_2 fluxes. This implies feedback mechanisms act inhomogeneously in different ocean regions. In the North Atlantic subpolar gyre, the simulated future cooling of SST improves the CO_2 gas solubility in seawater, and hence reduces the strength of positive climate-carbon cycle feedback in this region. In most of the ocean regions, the changes in Revelle factor is dominated by changes in surface pCO_2, and not by the warming of SST. Therefore, the solubility feedback is more prominent than the buffer capacity feedback. In our climate change simulation, the opening of Southern Ocean sea ice due to melting allows an additional ~20 Pg C uptake as compared to the simulation without climate change.

1 Introduction

Understanding the interactions between climate and the global carbon cycle is crucial to accurately project future climate change. Unfortunately, empirical evidence for global climate-carbon cycle interactions as well as their feedbacks for time scales relevant to

the current climate change (i.e., decadal to centennial time scales) is very limited. Therefore, such an assessment has to be attempted by applying comprehensive, fully interactive global climate-carbon cycle models (Heimann and Reichstein, 2008). Recently, state-of-the-art coupled climate carbon cycle models have been used as key elements in understanding present and future climate change. They include sophisticated interactions between the atmosphere, ocean circulation and marine biogeochemical cycles, terrestrial biosphere as well as sea-ice. Previous intercomparisons (Friedlingstein et al., 2006) have proven that these models, despite their notable uncertainties, are essential in predicting future interactions and feedbacks between climate-carbon components in the complex earth system.

The Bergen Climate Model "BCM" (Furevik et al., 2003) is a coupled atmosphere ocean general circulation model (AOGCM) that has been well-tested for both mean and transient climate conditions. It is generally able to capture the main features of the observed short- and long-term climate variability, such as the radiative forcing, freshwater fluxes, ENSO, NAO modes within realistic temporal and spatial variability. In addition, the BCM has been applied to integrate past climate scenarios for the United Nations Intergovernmental Panel on Climate Change (UN-IPCCv4) report (Randall et al., 2007). Nevertheless, the BCM has so far been a purely physical AOGCM lacking oceanic and terrestrial carbon cycle components necessary for the inclusion of carbon cycle feedbacks in future climate projections.

In this study, we coupled terrestrial and oceanic carbon cycle models to the BCM, creating the BCM-C. The model is applied to simulate climate-carbon cycle projections for the period 1850–2100. The simulations are compared with observations and validated towards other earth system model projections. Furthermore, we analyze the regional variability of mechanisms responsible for controlling the local and global climate carbon cycle feedback.

The manuscript is organized as follows, Sect. 2 describes the different model components used in this study as well as our coupling strategy, Sect. 3 describes the configuration and settings adopted in the model simulations performed, Sect. 4 sum-

marizes the results of the model simulations, and finally the manuscript is closed with discussions and conclusions.

2 Model description

The BCM-C consists of global atmospheric and oceanic general circulation model coupled to oceanic and terrestrial carbon cycle models. The newly coupled model is able to simulate interactively the known global carbon cycles processes, which include the radiative feedback necessary for climate change simulations. Each component of the BCM-C is described in more detail in the following subsections.

2.1 Atmospheric circulation model

The atmosphere component is the spectral atmospheric general circulation model ARPEGE from Météo-France (Déqué et al., 1994). The ARPEGE model as applied in this study is described in detail in Furevik et al. (2003), and its major features are briefly summarized here.

In ARPEGE, the representation of most model variables is spectral (i.e., scalar fields are decomposed on a truncated basis of spherical harmonic functions). In the present study, ARPEGE is run with a truncation at wave number 63 ($T_L 63$), and a time step of 1800 s. the grid point calculations are done with a grid of horizontal resolution of about $2.8^\circ \times 2.8^\circ$. A total of 31 levels is employed, ranging from the surface to 0.01 hPa (20 layers in the troposphere).

The physical parameterization is divided into several explicit schemes, which each calculate the flux of mass, energy and/or momentum due to a specific physical process. Different from the model description in Déqué et al. (1994), the version used in BCM contains a convective gravity drag parameterization (Bossuet et al., 1998), a new snow scheme (Douville et al., 1995), increased orographic drag (Lott, 1999) and modifications in deep convection and soil vegetation schemes. Importantly, a more adequate

turbulence scheme has been applied in this version for very stable cases (i.e., large Richardson numbers).

2.2 Oceanic circulation model

The ocean component is the Miami Isopycnic Coordinate Ocean Model (MICOM) based on (Bleck et al., 1992) with the following updates. The original MICOM uses potential density with reference pressure at 0 db as vertical coordinate (σ_o-coordinate). This ensures that the very different flow and mixing characteristic in neutral and dianeutral directions is well represented near the surface since isopycnals and neutral surfaced are similar near the reference pressure. For pressure levels that differ substantially from the reference pressure, this does not hold. Here, a reference pressure of 2000 db is used. The non-neutrality of the isopycnals in the world ocean is then reduced compared to having the reference pressure at the surface (McDougall and Jackett, 2005).

Furthermore, for tracer advection and layer thickness, the current MICOM uses incremental remapping (Dukowicz and Baumgardner, 2000) adapted to the grid staggering of MICOM. The algorithm is computationally rather expensive compared to other second order methods, but the cost of adding additional tracers is modest. In contrast to the original transport method, incremental remapping ensures monotonicity of the tracers.

Traditionally, MICOM expresses the pressure gradient force (PGF) as a gradient of a potential on an isopycnic surface, as such formulation has favorable numerical properties (Hsu and Arakawa, 1990). This, however, is only accurate if the density can be considered as a function of potential density and pressure alone, which is not the case (de Szoeke, 2000). The PGF formulation used in the current version is based on the formulation of Janic (1977) where the PGF is expressed as a gradient of the geopotential on a pressure surface, which allows a more accurate representation of density fields.

The treatment of diapycnic mixing follows the standard MICOM approach of a back-

ground diffusivity dependent on the local stability and is implemented using the scheme of McDougall and Dewar (1998). To incorporate shear instability and gravity current mixing, a Richardson number dependent diffusivity has been added to the background diffusivity. This has greatly improved the water mass characteristics downstream of overflow regions. Lateral turbulent mixing of momentum and tracers is parameterized by Laplacian diffusion, and layer interfaces are smoothed with biharmonic diffusion.

With the exception of the equatorial region, the ocean grid in our configuration is almost regular with horizontal grid spacing approximately 2.4°×2.4°. In order to better resolve the dynamics near the equator, the horizontal spacing in the meridional direction is gradually decreased to 0.8° along the equator. The model has a timestep of 4800 s and a stack of 34 isopycnic layers in the vertical coordinate, with potential densities ranging from 1029.514 to 1037.800 $kg\,m^{-3}$. A non-isopycnic surface mixed layer on top provides the linkage between the atmospheric forcing and the ocean interior.

2.3 Sea-ice dynamical model

The original sea-ice model integrated into MICOM is a dynamic and thermodynamic sea-ice model. It shares the same horizontal grid resolution and the heat, salt, and water flux exchanges between the ocean and sea-ice are handled internally. The thermodynamic part of the sea-ice model is based on Drange and Simonsen (1996). The model consists of one ice and one snow layer assuming a linear temperature profile in each layer. The temperature profile is determined by the freezing temperature at the water/ice boundary, and the balance between turbulent, radiative and conductive heat fluxes at the snow/air boundary. The dynamical part of the sea-ice model uses viscous-plastic rheology based in the implementation of Harder (1996).

In addition to the original sea-ice model, a multi-category sea-ice model, GELATO, can also be selected as the sea-ice component. The GELATO categorizes different ice slabs based on variety thicknesses, which allows a more precise treatment of thermodynamics and therefore ice growth rates for different ice categories. Within a grid cell, sea ice is described as a collection of ice slabs, described by its thickness, the fraction

of model grid it covers, its enthalpy, and the amount of snow cover. A more detailed description of GELATO can be found in Salas-Melia (2002).

In this study, the original sea-ice model originally implemented within MICOM is applied. The large scale climate state and variability modes simulated by BCM using the GELATO sea-ice model are discussed in Otterá et al. (2009).

2.4 Ocean carbon cycle model

The BCM-C adopts the Hamburg Ocean Carbon Cycle (HAMOCC5.1) model, which is based on the original work by Maier-Reimer (1993) with the extensions of Maier-Reimer et al. (2005). The current version of the model includes an NPZD-type (nutrient, phytoplankton, zooplankton, and detritus) ecosystem model following Six and Maier-Reimer (1996) with multi nutrient co-limitations (Aumont et al., 2003). The model contains over 30 biogeochemical tracers, which include dissolved inorganic carbon, total alkalinity, oxygen, nitrate, phosphate, silicate, iron, phytoplankton, and zooplankton. In addition to temperature, and light, the primary production is also co-limited by nitrate, phosphate, and iron concentrations. Fixed Redfield ratios (i.e., P:N:C:Δ O_2) are used for production and remineralization of biogenic matter. Phytoplankton growth is formulated according to the Michaelis-Menten kinetics. Two major classes of phytoplankton functional groups are simulated in the model: diatoms and coccolithophores. The diatom fraction of the total phytoplankton is computed as a function of silicate concentration, where higher silicate concentrations yields higher diatom concentration. The remaining phytoplankton is assumed to be coccolithopores. In the tropical oligotrophic, nitrate depleted regions, the marine ecosystem module accounts for atmospheric nitrogen fixation essential for cyanobacteria growth. Particulate organic carbon produced due to the ecosystem dynamics are exported out of the euphotic zone with a constant sinking speed. Once exported, the organic matter is remineralized at depth, and the non-remineralized particles are collected by the sediment.

The inorganic carbon chemistry in the HAMOCC5.1 model is following Maier-Reimer and Hasselmann (1987). The surface pCO_2 in the model is computed prognostically as

a function of alkalinity, total DIC, temperature, pressure, and salinity. The dissolution of calcium carbonate at depth is computed as a function of carbonate ion saturation state and a constant dissolution rate. The air–sea gas (i.e., CO_2 and O_2) exchange processes are formulated as a function of gas solubility, transfer velocity, and the difference between partial pressure tracers in air and water following Wanninkhof (1992). The gas tracer solubilities are computed according to Weiss (1970) and Weiss (1974), whereas the gas transfer velocity depends on the Schmidt number and prognostic wind speed on the surface. Also note that the model has a 12-layer sediment model, which is applicable for future, long-term model studies, for example where the buffering of anthropogenic CO_2 through calcium carbonate dissolution from the seafloor becomes important.

2.5 Terrestrial carbon model

The Lund-Postdam-Jena Model (LPJ) (Sitch et al., 2003) is a large-scale terrestrial carbon cycle model, which includes global dynamical vegetation. It implements terrestrial photosynthesis, respiration, resource competition, tissue turnover, dynamic vegetation population with 10 plant functional types (PFTs), soil organic and litter dynamic as well as natural fire occurence. The soil hydrology, with 2-level soil moisture, is treated by LPJ (i.e., no direct coupling to ARPEGE). For each model grid, carbon storage is allocated into four compartments, vegetation, litter, fast and slow overturning soil carbon pool. The current version of the model does not include land use change. The LPJ has a horizontal resolution of approximately 2.5°×2.5° with monthly model timestep. The 2.5° resolution corresponds to the atmospheric model, as they run on the same grid (over land).

2.6 Coupling strategy

The OASIS coupler (Terray et al., 1995), which has been developed at the National Centre for climate modelling and global change (CERFACS), Toulouse, France, has

been used to couple ARPEGE with MICOM. OASIS synchronizes different model components, such that the fastest running model can wait for the other until all components are integrated at a complete prescribed time interval (i.e., one day). It also efficiently reads, interpolates, and transfers the exchange fields between ARPEGE and MICOM.

The HAMOCC5.1 is coupled directly into MICOM and therefore has identical temporal, horizontal, and vertical resolutions. This coupling allows all biogeochemical tracers within HAMOCC5.1 to be advected along MICOM's isopycnal coordinates, which resemble the real structure of water column and avoid artificial mixing and advection in the ocean interior. The caveat of such coupling includes problem with massless layers in the outcrop regions and introduction of bulk mixed layer on the model topmost layer. The marine biological production occurs within the euphotic zone, which is formulated to be the minimum between 90 m depth and the mixed layer depth simulated by MICOM. The biogeochemical tracers are advected by the prognostic physical fields simulated by MICOM. In addition, variables such as temperature, salinity, pressure, and density used in the computation of ocean pCO_2, pH, and carbonate ion fields are also taken from MICOM. More detail on HAMOCC-MICOM coupling, together with series of sensitivity carbon cycle studies are discussed in Assmann et al. (2009).

The LPJ is integrated annually at the end of each model year, and forced by monthly ARPEGE output fields of temperature, precipitation, cloud coverage, and number of rainy days per month. The number of wet days per month is used to run an internal weather generator, since part of the LPJ code runs at a daily time-step. The coupling of CO_2 gas exchange occurs at the end of every model year, where an updated atmospheric CO_2 concentration is computed based on the annual fluxes between the atmosphere and the ocean or land. Thus, the atmospheric CO_2 concentration is only updated once a year for the land and ocean. Currently, the albedo feedback due to changes in the terrestrial PFT is not implemented, but it is part of our future research plans. In all of the model simulations, no form of flux adjustments is applied to the model.

3 Model simulations

A set of three model simulations adopting different configurations and forcing fields was carried out. The first is designed to analyze and evaluate the steady state simulated by the model, whereas the latter two are intended to analyze in detail the climate-carbon cycle feedback in the model.

3.1 Experiment REF

The REF model simulation is performed for spin up. The fully coupled BCM-C is integrated for 600 years applying constant pre-industrial atmospheric CO_2 concentration at 284.7 ppm. The goal of the REF simulation is to generate a pre-industrial (i.e., 1850 A.D.) steady state climate, which can be used for the initial state of COU and UNC simulations (see below).

3.2 Experiment COU

For the second simulation, the BCM-C is initialized based on REF steady state and integrated from year 1850 to 2100 forced only by anthropogenic CO_2 emissions. For the period of 1850–1999, carbon emissions based on observed records of fossil fuel burning and deforestation (Marland et al., 2005) are used, whereas for the period 2000–2100, the IPCC SRES-A2 emission scenario (Houghton and Hackler, 2002) is used.

3.3 Experiment UNC

The third model simulation is similar to the COU simulation, but the radiative effect of atmospheric CO_2 change is removed in the model. Therefore unlike in COU, the simulated carbon cycle in UNC experiences no climate change effect (e.g., warming, change in ocean atmosphere and ocean circulation, etc.). Experiment UNC was designed such that its difference with experiment COU represents the pure climate feedback on the carbon cycle system. This set-up is similar to that of the C4MIP study

(Friedlingstein et al., 2006).

4 Results and evaluation

4.1 Preindustrial reference run

In general, the spin-up experiment (REF) is able to reach a steady climate state, which is to a large degree consistent with observations. The performance of spatially-averaged climate parameters simulated by BCM-C in REF is compared to the observed climatology state and summarized using a Taylor diagram as shown in Fig. 1. The Taylor diagram evaluates the model performance as a function of normalized standard deviation, centered root-mean-square (RMS), and pattern correlation (Taylor, 2001). All simulated variables are normalized by the respective observed variable's standard deviation, thus a perfect model-data fit would reside in the observation point (i.e., σ=1, RMS=0, and r=1). The model is able to reproduce the observed 2-m surface air temperature (SAT) and sea surface temperature (SST) quite realistically in terms of spatial and actual amplitude variabilities, shown by the correlation and normalized standard deviation close to unity. The simulated surface salinity (SSS) deviates noticeably from the observation with normalized standard deviation of only 0.5. This discrepancy is mainly due to the overestimated Arctic water salinity in the model compared to the LEVITUS climatology SSS. The simulated precipitation PR and mean sea level pressure SLP variability are comparable to the observations. Biases in the precipitation are mainly due to weaker precipitation rate over the ocean than that observed, whereas misfit between the observed and modelled mean sea level pressure is caused by excessive high pressure over the Arctic, which resulted in weaker Icelandic and Aleutian low pressure systems. Additionally, the atmospheric meridional pressure gradient in the Antarctic circumpolar region is too weak. This resulted in weak surface winds there.

The marine carbon cycle in REF run produces the observed main characteris-

tics of ocean biogeochemistry, which includes global distributions of nutrients, DIC, alkalinity, High Nutrient-Low Chlorophyll regions, regional net primary production, and air-sea CO_2 fluxes. The preindrustrial ocean tracer distribution simulated by HAMOCC5.1 is discussed in Assmann et al. (2009). Within the last 100 model years of the spin-up run, the ocean carbon cycle yields steady annual air-sea CO_2 fluxes, net primary production, particle organic carbon export, and calcite export of 0±0.2, 39±2.0, 9.5, and 0.6 Pg C yr^{-1}, respectively (see supplemental Fig. 1 http://www.geosci-model-dev-discuss.net/2/845/2009/gmdd-2-845-2009-supplement.pdf). The model simulates well the fundamental characteristics of oceanic CO_2 fluxes patterns, with dominant outgassing in the Equatorial Pacific and uptakes in the North Atlantic, and the Southern Ocean.

The interannual land-atmosphere carbon fluxes simulated in REF has maximum variability range of ±2.0 Pg C yr^{-1}. The preindustrial equilibrium global terrestrial vegetation, soil, and litter carbon content simulated by BCM-C are 735, 1380, and 145 Pg C, respectively, consistent with the range of other terrestrial model studies (Kucharik et al., 2000; Sitch et al., 2003) (see also supplemental Fig. 2 http://www.geosci-model-dev-discuss.net/2/845/2009/gmdd-2-845-2009-supplement.pdf).

4.2 Model projections of global carbon cycle and climate change

The projected modern-period anthropogenic carbon uptake simulated in the fully coupled run compare reasonably well with estimates from other studies. For example, during the 1990s, the model simulates annual mean of terrestrial and oceanic carbon sink of 1.73 and 2.36 Pg C yr^{-1}, respectively. These values are well within range of independent multi-models studies and observation-based estimates (Cramer et al., 2001; Takahashi et al., 2009). The spatial anthropogenic carbon uptake by the ocean simulated by the BCM-C is shown together with the observation-based estimates from Sabine et al. (2004) in Fig. 2. Here, the anthropogenic carbon storage is computed from the difference between carbon inventories from year 1994 and the averaged annual pre-industrial state. Globally, the time-integrated anthropogenic carbon uptake

up to year 1994 is estimated to be 107 Pg C of this amount, the North Atlantic region (>15° N) account for 32%, whereas the regions south of −14° S account for 48% of the global inventory. In general, the simulated regional anthropogenic carbon uptake is slightly stronger in the North Atlantic region, along the Gulf Stream. This uncertainty may be attributed to the artificially large mixed layer depth that allow surface carbon to be transported into deep ocean more efficiently (Assmann et al., 2009). This overestimation is damped by slightly lower carbon uptake in the rest of the world ocean regions. For the same period, the terrestrial counterpart take up approximately 90 Pg C. The values above are well within error ranges given in Sabine et al. (2004) study.

The BCM-C model reproduces relatively well the observed atmospheric CO_2 concentration (i.e., 390 ppm for the present day value). In the fully coupled simulation (COU), the atmospheric CO_2 concetration is projected to increase to 898.5 ppmv by 2100, whilst in the uncoupled (UNC), it increases only to 784.6 ppmv (see Fig. 3). The projected atmospheric CO_2 concentration and the difference between COU and UNC is well within the range given by 11 earth system model forecasts, as shown in Fig. 3 (Friedlingstein et al., 2006).

Because the atmospheric CO_2 change in the UNC simulations has no radiative effect, projected temperature variability remains within the preindustrial state. In the COU simulation, the model projects an increase in global average surface atmosphere and ocean temperature by roughly 3.5° and 2.5° C, respectively as shown in Fig. 4. Based on the changes in global surface atmosphere temperature, the climate sensitivity of the model, defined as the ratio of changes in global temperature to changes in atmospheric CO_2, is 0.0057°C/ppm. This value is also within range of 0.0038–0.0082°C/ppm obtained from the other earth system models (Friedlingstein et al., 2006).

Changes in global temperature, in turn, alter key features of the climate system, e.g., ocean circulation, sea-ice extent, precipitation, solar radiation, and surface winds. These changes in fundamental climate parameters modify both the terrestrial and ocean carbon cycle, and finally feedback to atmospheric CO_2 concentration and the climate system. To first order, an increase in global temperatures would reduce the

average rate of carbon uptake by the terrestrial reservoir as well as the ocean. The "gain" of the climate-carbon feedback can be computed based on the methodology of Friedlingstein et al. (2006),

$$g = 1 - \frac{\Delta C_A^{\mathrm{unc}}}{\Delta C_A^{\mathrm{cou}}}, \quad (1)$$

where $\Delta C_A^{\mathrm{unc}}$ and $\Delta C_A^{\mathrm{cou}}$ represent the change in atmospheric CO_2 in the UNC and COU runs, respectively. Here, the g simulated by our model is equal to 0.18 (the average of other models is 0.15), indicating a positive feedback of the climate system. The regional difference in the climate-carbon cycle feedback as well as the fundamental mechanisms controlling them are discussed in more detail in the following subsections.

In both the COU and UNC experiments, the model simulates a continuous increase in atmospheric carbon uptake by the ocean, with annual uptake of 2.3 Pg C/yr for the present-day climate and up to 6 Pg C/yr uptake by year 2100. This increase in oceanic carbon uptake is expected as the difference between the partial pressure of CO_2 in the atmosphere and ocean surface also continues to increase. Nevertheless, the fraction of the annual CO_2 emission taken up by the ocean decreases, implying that the ocean may be close to its carbon saturated state. In the COU simulation, the terrestrial carbon uptake reaches its maximum by the middle of the 21st century of 4.5 Pg C/yr and decreases afterwards down to 1.7 Pg C/yr by the end of this century. In the UNC simulation, where the climate change effect is suppressed, the terrestrial carbon uptake shows no significant decreasing trend, with maximum carbon uptake of nearly 7 Pg C/yr by year 2100. The significant difference in the terrestrial carbon uptake between the COU and UNC simulation suggest that the positive global climate–carbon cycle feedback is mainly attributed by the terrestrial processes. Both the simulated annual ocean and terrestrical carbon uptakes look very reasonable, located well in the middle of other model estimates.

The COU simulations also show a reduction in the strength of the Atlantic Meridional Overturning Circulation (AMOC) from 21 to 15Sv by year 2100. This change, consistent

with a multi-GCMs study by Schmittner et al. (2005), resulted in only a small reduction in the marine primary production and export production, especially in the high latitude regions. Earlier studies show that the slow down in the overturning circulation may have little oceanic carbon cycle-climate feedback for the short-period pertinent to this study. For example, Zickfeld et al. (2008) summarizes that up to 2100, the increase in SST in the warmer climate, which reduces the CO_2 solubility is mostly responsible for the reduction in the carbon uptake. Note that increase in SST also decrease the CO_2 buffer factor (i.e., buffer capacity increases with rising T) for seawater. However, changes in carbon uptake due to chnages in solubility is probably stronger. For multi-century time scales, the AMOC and ocean circulation is generally found to be the main reason for reduced CO_2 uptake. For these longer time scales, the weakening of AMOC reduces the fluxes of upwelled nutrients to the surface, which in turn reduces the carbon uptake by the biological pump.

4.3 Terrestrial climate-carbon cycle feedbacks

All previous coupled climate-carbon cycle models reported in the literature unanimously demonstrate a positive feedback between terrestrial carbon cycle and climate change, mainly due to the consequences of kinetic sensitivity of photosynthesis and respiration to temperature (Luo, 2007). Figure 3c shows that the global terrestrial climate-carbon cycle feedback simulated by our model is also positive, resulting in less uptake of approximately 262 Pg carbon when climate change is taken into account. The feedback strength in the model is controlled primarily by the response of terrestrial photosynthesis and respiration to changes in different climate variables, such as temperature and atmospheric CO_2 concentration. Here, we will assess the regional strength of the terrestrial climate-carbon cycle feedback by computing the sensitivity of regional carbon uptake, net primary production, and respiration dynamics to changes in atmospheric CO_2 concentration as well as surface temperature.

While an increase in atmospheric CO_2 would generally amplify terrestrial carbon uptake due to CO_2 fertilization, the associated climate change effect on regional ter-

restrial carbon cycle is less understood and predictable. The geographical distribution of time-integrated terrestrial carbon uptake by year 2100 from the COU experiment is shown in Fig. 5a. By the end of the century, regions that remain prominent net carbon sinks are the equatorial regions, central and northern Asia, central Europe, and northern America. In the tropics, significant carbon uptake is mainly attributed to an increase in atmospheric CO_2 due to the fertilization effect. At high latitudes, in addition to CO_2 fertilization, an extended growing season also leads to an increase in NPP. However, in certain regions (i.e., northeastern Europe, northern and central America, and eastern Asia), where winter temperature increase significantly by as much as 20°C, soil respiration overcomes the NPP increase, resulting in a reduced soil turnover time. These regions, in contrast, have a very pronounced positive climate-carbon feedback and a strong outgassing of carbon to the atmosphere by the end of the 21st century. Figure 5b shows the difference in accumulated carbon uptake between the COU and UNC simulations. To a first order, regions with negative values represent regions with positive climate-carbon cycle feedback. Some regions, such as the equatorial Africa, Amazonia, and southeastern Australia, take up carbon initially in the early simulation periods, but end up releasing more carbon by the end of the 21st century. The main reason for the outgassing of the tropical regions mentioned above is the reduction in NPP due to warming (see the regional sensitivity of NPP to temperature change in Fig. 6). This sensitivity is in line with study by Sitch et al. (2008). Figure 5b also shows that there are a few temperate terrestrial biospheres domains along 30° N and 20° S that take up more carbon when climate change is included in the model simulations, inducing a negative climate-carbon cycle feedback.

Following Friedlingstein et al. (2006), the sensitivity of terrestrial carbon uptake to atmospheric CO_2 can be expressed as:

$$\beta_L = \frac{\Delta C_L^{\mathrm{unc}}}{\Delta C_A^{\mathrm{unc}}}, \tag{2}$$

where $\Delta C_L^{\mathrm{unc}}$ and $\Delta C_A^{\mathrm{unc}}$ represent the change carbon contents in the land and at-

mosphere, respectively, over a given period simulated in the UNC experiment. The latitudinal variability of β_L is shown in Fig. 6a. It shows that the response of carbon uptake due to increase in atmospheric CO_2 alone is generally strongest in the equatorial regions and decreasing toward higher latitude regions. Since carbon uptake in our model is computed mainly as the difference between NPP and respiration, the sensitivities of these terms to CO_2 concentration is also computed. Generally, Fig. 6b also shows that NPP at low latitudes has the strongest CO_2 fertilization effect. The sensitivity variation between different latitudes is to some extent contributed by temperature variabilities. The study by Farquhar et al. (1980) demonstrates that the assimilation rate of CO_2 is more efficient in warmer temperatures. Analogously, Hickler et al. (2008) show that the effect of CO_2 enhancement on regional plant photosynthesis is strongest at higher temperature regions.

Interestingly, the latitudinal response of soil respiration to CO_2 changes is very similar to the response of NPP, in that higher ambient CO_2 concentrations leads to higher soil respiration rates. The effect of CO_2 fertilization on heterotrophic respiration can be explained as follows. Higher atmospheric CO_2 levels reduce stomatal opening and hence reduce evapotranspiration. This condition leads to increase in water usage efficiency and increasing soil water moisture. In addition, increase in NPP also leads to increase in litter input to the soil in some regions. Finally, these factors lead to an increase in soil respiration. In the low latitudes, the strong sensitivity simulated by the model is mainly due to the warm tropical temperatures and significant increase in soil moisture. At high latitudes, despite increase in litter carbon as well as soil moisture, the soil decomposition remains low in the high CO_2 environment, which may be due to the lower temperature.

In order to analyze the sensitivity of regional carbon uptake to changes in temperature alone, an additional experiment (UNCb) was performed by only running the LPJ model offline. In this experiment, the LPJ is simulated for the same period, forced by the climate variability from the COU simulation while maintaining constant, preindustrial atmospheric CO_2 concentration. Similar to Eq. (2), the sensitivity of carbon uptake

to changes in temperature can be computed as:

$$\gamma_L = \frac{\Delta C_L^{\text{uncb}}}{\Delta T^{\text{cou}}}, \quad (3)$$

where ΔC_L^{uncb} and ΔT^{cou} represent the change land carbon contents in the UNCb and change in surface temperature in the COU simulations, respectively. All regions show uniform sensitivity signs, increase in carbon outgassing with higher atmospheric temperature. Figure 6d shows that tropical regions have highest sensitivity towards changes in temperature, whereas the high latitude regions generally have lower sensitivity. In the northern hemisphere midlatitude (30° N–60° N), our simulation also shows relatively large climate-carbon cycle feedback, where future warming leads to reduction in the annual NPP and increase in heterotrophic respiration. This results in is line with independent study of Cramer et al. (2001), which uses multiple dynamical vegatation models to assess the terrestrial climate-carbon cycle feedback.

In general, higher temperatures affect the tropical regions by decreasing the annual NPP and have relatively small influence on the heterotrophic respiration. At high latitudes, increase in soil respiration due to warming overtakes the increase in NPP due to the extended growing seasons. This mechanism would eventually lead to a significant reduction in the soil carbon turnover time by up to 25 years (not shown here) in these regions. Figure 6e and f also show that the regional sensitivity of net primary production and heterothropic respiration to changes in temperature is very non-linear, perhaps due to variabilities of other physical forcings (i.e., precipitation) induced by changes in temperature.

4.4 Oceanic climate-carbon cycle feedback

The regional oceanic carbon uptake is determined by the gradient between the partial pressure of CO_2 in the atmosphere and surface ocean, where the latter term depends strongly on the physical state of the ocean, hence the climate variability. In order to

analyze the regional climate-carbon cycle feedback in the ocean, we compute the carbon uptake changes with respect to the preindustrial state, and compute the difference between the COU and UNC simulations. Figure 7a shows a map of time-integrated changes (1860–2100) in oceanic carbon uptake with respect to the average preindustrial (i.e., 1850–1859) state. In both model runs, the model simulates a net carbon uptake in nearly all ocean regions as a result of enhanced atmospheric CO_2 concentration. In addition, well-known outgassing regions have also switched into carbon sink regions. For example, the Equatorial Pacific absorbed as much as 4 kg C/m^2 by the end of model simulations. The oceanic carbon uptake through the end of the 21st century occurs mainly in the North Atlantic, northwestern Pacific, and in the Southern Ocean (South of 30° S). In these regions, substantial carbon fluxes into the ocean correspond to regions with pronounced winter mixing, which is an important mechanism to transport surface DIC to deeper ocean layer. Additionally, compared to the preindustrial state, the fully coupled simulation generates the largest changes in carbon fluxes in the Southern Ocean, where the anomaly of carbon uptake is as high as 10 kg C/m^2 over the entire model integration period (see Fig. 7a).

The difference between the COU and UNC simulations in the accumulated carbon fluxes to the ocean are shown in Fig. 7b. Negative values represent less carbon uptake when climate change is taken into account and, therefore, are considered as positive climate-carbon cycle feedback regions, whereas positive values represent the opposite. Negative patterns appear in the Southern Ocean (between 30° S and 50° S), North Atlantic and northwestern Pacific regions. Therefore, these regions are considered as strong positive climate-carbon cycle feedback regions. Positive values are most pronounced in the high-latitude Southern Ocean, the Arctic regions, southeast Australia, and in western boundary currents along the North Pacific and North Atlantic oceans.

Figure 6b also shows that the impact of climate change on regional CO_2 fluxes is spatially inhomogeneous. In order to analyze the temporal impact of climate change on carbon uptake in different ocean regions, we compute the difference (COU-UNC) in spatially integrated annual carbon uptake (shown in Fig. 8).

Except for the high latitude Southern Ocean, the effect of climate change in all other regions is generally not pronounced until the middle of the 21st century. In the Tropical Pacific, South Pacific and South Indian Oceans, changes in carbon uptake between both runs are well within the variabilities of the the first few decades, suggesting that the effect of climate change may not be significant for these regions. Possitive feedback mechanisms between climate and carbon uptake are evident in the North Pacific, Tropical Indian, and all parts of the Atlantic Ocean. Here, the COU simulation shows a reduction in carbon uptake as compared to the UNC simulation. By 2100, the model indicates a reduction of nearly 0.4 Pg yr^{-1} of carbon uptake in the Atlantic Ocean, attributed to climate change.

In both polar regions (i.e., ARC and SOC), an increase in the carbon uptake due to climate change is simulated. The signal in the Arctic shows an increased temporal variability toward higher carbon uptake in the future, but the amplitude is relatively small as compared to that of the Southern Ocean. In the Southern Ocean, the effect of negative feedback mechanisms starts to show up in the 1970s. By the end of the 21st century, the Southern Ocean would have taken up ~0.3 Pg C yr^{-1} more when climate change is included in the model simulation. Here, substantially more carbon uptake is simulated partly due to the melting of sea ice. We note that the BCM-C model generates biases due to stronger mixing in this region, allowing the sea ice to almost disappear in the summer period. Figure 9 shows that most of the difference between carbon uptake in the COU and UNC simulations occurs within or close to the areas, where the sea ice has retreated. The opening of areas due to the sea ice melting allows an additional uptake of approximately 20 Pg carbon between year 2000 and 2100.

In order to better understand the feedback mechamisms in the other regions, we compute the effect of different key climate factors controling the air-sea CO_2 fluxes in the model. Here, the flux of carbon between the atmosphere and the ocean interface is defined as follow:

$$F_{CO_2} = \alpha \cdot K \cdot \Delta pCO_2, \quad (4)$$

where α is the solubility of CO_2 gas in the seawater computed as a function of seawa-

ter temperature and salinity according to Weiss (1974), K is the gas transfer velocity, which depends on the surface wind speed and Schmidt number according to Wanninkhof (1992), and ΔpCO_2 is the difference in partial pressure of CO_2 between the atmosphere and the ocean.

Following the study by Crueger et al. (2008), the effect of changing solubility, gas transfer rate, and partial pressure difference in controling changes of CO_2 fluxes differences between the COU and UNC simulation can be estimated as:

$$\Delta F_S = \Delta\alpha \cdot \overline{K} \cdot \overline{\Delta pCO_2} \quad (5)$$

$$\Delta F_K = \overline{\alpha} \cdot \Delta K \cdot \overline{\Delta pCO_2} \quad (6)$$

$$\Delta F_{\Delta pCO_2} = \overline{\alpha} \cdot \overline{K} \cdot \Delta(\Delta pCO_2), \quad (7)$$

where the actual changes in air-sea CO_2 fluxes between the two simulations is approximately equal to the sum of the three terms above,

$$\Delta F_{CO_2(COU-UNC)} \approx \Delta F_\alpha + \Delta F_K + \Delta F_{\Delta pCO_2}. \quad (8)$$

In the above equation, "Δ" represents the difference of the mean and and "–" represents the mean of the denoted terms from the COU and UNC simulations. Here, we only compute the difference and average for the period of 2080–2099 since the largest changes between the two simulations occur within this period (see also Fig. 8). Figure 10 shows the map of changes of oceanic carbon uptake attributed to these different terms (based on Eqs. 5, 6, and 7) together with the actual difference of simulated carbon uptake between the two runs (i.e., left-hand side of Eq. 8).

In the model, solubility of gaseous CO_2 in seawater is predominantly determined by SST and secondarily by surface salinity, where higher SST and higher salinity both lead to lower solubility. On contrast, lower SST and lower salinity lead to higher solubility. As shown in Fig. 4, simulated climate change in the COU simulation increases SST by approximately 2.5°C globally. However, most of this warming occurs within high latitude

regions (i.e., Southern Ocean, northwest Pacific, North Atlantic, and the Arctic), which leads to a reduction of CO_2 solubility. In contrast, in the North Atlantic subpolar gyre, there is a slight increase of solubility due to cooling of approximately 2°C change in SST. We attribute this cooling of SST to the reduction of lateral heat fluxes from the warm subtropical water in connection to the slowdown of AMOC strength. This is consistent with an earlier study by Mikolajewicz et al. (2007). In the Southern Ocean, the reduction in solubility pattern also reflects a pattern of SST increase caused by climate change. Maximum SST increases by as much as 7°C are simulated along latitude 60° S of the Indian and Atlantic Ocean sections. Consequently, we see similar patterns in the reduction of carbon uptake due to lower solubility (see Fig. 10a). Consistent with the study by Crueger et al. (2008), our model produces little or negligible changes in surface solubility in the Equatorial Pacific, despite a regional sea surface warming of 3°C. This is due to the fact that the solubility changes are less significant in warmer than colder environments (Weiss, 1974).

The CO_2 gas transfer velocity in the model is mainly proportional to the fraction of sea ice coverage and the square of surface wind speed, but it also depends on the SST. Thus, higher wind speeds and lower surface temperatures lead to a faster transfer rate of CO_2 gas into or out of the ocean. An increase in carbon uptake due to increased gas transfer velocities predominantly occurs in the Southern Ocean along the 60° S latitude band. Whilst there is increase (i.e., by approximately 30%) in zonal average near surface wind speed along 60° S latitude, a significant increase in gas transfer velocity is mainly attributed to the retreat of the average sea ice from approximately 55° S to >60° S (see also Fig. 9). Also note that the HAMOCC5.1 model treats sea ice as an impermeable lid, thus the fraction of sea ice in the model grid is a determining factor for air-sea gas exchange. In the North Atlantic subplolar gyre, there is a small, but noticeable reduction in wind stress, which slightly reduces the carbon uptake in this region as shown in Fig. 10b.

Despite large spatial variabilities in the factors determining regional carbon uptake mechanism, Fig. 9c and d show that differences in carbon uptake between the COU

and UNC simulations mainly resemble the effect of changes in partial pressure CO_2 difference between the atmosphere and the ocean. Since the atmospheric CO_2 concentration in the model is represented as a bulk annual averaged value, the spatial variability in ΔpCO_2 is simply determined by the spatial surface ocean pCO_2 pattern. Surface pCO_2 in the model is predominantly controlled by the surface DIC. The surface DIC concentration is, in turn, determined by regionally and temporally varying biophysical processes such as the ocean circulation, biological activity, and convective mixing (Tjiputra and Winguth, 2008). Additionally, pCO_2 also depends on surface alkalinity, salinity, and temperature. In large portions of the low latitue regions (30° N–30° S), there are little differences in the ΔpCO_2 in the COU and UNC simulations. In the North Atlantic (between 30° N–60° N), the ΔpCO_2 simulated in the COU run is lower than that of the UNC run. This difference is potentially due to weaker winter mixing processes (i.e., the average mixed layer depth decreases by as much as 100m in the simulation with climate change), which is the dominant mechanism for transporting CO_2 from the surface to the deep ocean and maintaining lower surface DIC concentrations. In the North Pacific, noticeably lower carbon uptake due to lower ΔpCO_2 is simulated in COU. In contrast to the North Atlantic, the changes in mixed layer depth signals in this region are insignificant. Therefore, the 4°C warmer SST may be the reason for lower ΔpCO_2 simulated in COU. Note that warmer SSTs would yield a higher partial pressures of CO_2 despite similar surface DIC concentrations. Warming over the Southern Ocean between 30° S and 60° S lowers the average mixed layer depth and increases the surface pCO_2 in the COU. However, in regions where the warming causes the sea ice cover to disappear (South of 60° S), the model simulates an increase of the average mixed layer depth, by as much as 100 m, as compared to the simulation without climate change.

In terms of the global carbon budget, Fig. 10 also indicates that the consequences of the three climate parameters in altering oceanic carbon uptake are of the same order of magnitude. This suggests that the climate induced changes in CO_2 solubility, gas transfer rate, as well as ΔpCO_2 are of equal importance in regulating the feedback

mechanism.

The above analysis shows that warming will reduce the solubility of CO_2 gas in seawater. However, note that increase in water temperature will also reduce the Revelle factor (i.e., increase the buffer capacity), through a better dissociation of CO_2 into bicarbonate and carbonate. On the other hand, the Revelle factor increases with rising pCO_2 (Zeebe and Wolf-Gladrow, 2001). The Revelle factor measures the changes of partial pressure of CO_2 in seawater for a given change in DIC. Hence, for a given increase in atmospheric CO_2 concentration, ocean waters with low values of the Revelle factor has higher oceanic equilibrium concentration of DIC than ocean waters with high Revelle factor (Sabine et al., 2004). In order to estimate the changes in Revelle factor due to climate change (i.e., increase in SST) as well as due to increase in surface pCO_2, we compute the difference between the Revelle factor for year 2099 and year 1850 from the COU and UNC simulation, as shown in Fig. 10a and b. Generally, there is an agreement in increasing Revelle factor in the future, hence lower buffer capacity of seawater to take up CO_2. For most of the region, Fig. 11b resemble well the spatial pattern of Fig. 11a. This suggests that future changes in Revelle factor is dominated by changes in surface pCO_2. In several high latitude regions, such as northwestern Pacific and the Southern Ocean (south of 60° S), the simulated warming in SST of as much as 5° C maintain the Revelle factor similar or slightly lower than that of the preindustrial period. In addition, we can estimate the future changes in Revelle factor attributed to only climate change by compute the difference in Revelle factor between COU and UNC simulation for year 2099 (Fig. 11c). Figure 11c demonstrates that warming in parts of the Southern Ocean and nortwestern Pacific induce lower Revelle factor. On the other hand, cooling in the North Atlantic subpolar gyre slightly increase the Revelle factor in that region.

5 Discussions and conclusions

In this study, we couple terrestrial (LPJ) and oceanic (HAMOCC5) global carbon cycle modules into the Bergen Climate Model (BCM). Our results show that the BCM-C model is able to simulate relatively well the temporal and spatial variabilities of the observed present climate and carbon cycle processes. The simulated future projection of atmospheric CO_2 concentration as well as global oceanic and terrestrial carbon uptake lies well within range of other earth system models. Nevertheless, note that the current model does not allow the terrestrial vegetation to feedback to the atmosphere by changing the surface albedo. The model also ignores the terrestrial nitrogen cycle and the spatial variability of atmospheric CO_2 concentrations.

The fully coupled climate-carbon cycle model (BCM-C) is integrated for the period 1850–2100 and forced by prescribed historical and IPCC SRES-A2 CO_2 emission scenarios. In order to assess the mechanisms controlling the climate-carbon cycle feedback, two model simulations were generated, one where the climate change effect is included and one where it is suppressed. According to previous studies using complex three-dimensional earth system models (Cox et al., 2000; Friedlingstein et al., 2006; Mikolajewicz et al., 2007), it is well accepted that future climate change is likely to reduce carbon uptake, retaining a larger fraction of airborne CO_2 in the atmosphere. Our model simulations also show a decrease in the strength of carbon uptake, predominantly by the terrestrial reservoir, despite a continuous oceanic carbon uptake towards the end of the 21st century. The oceanic carbon uptake rate, however, slows down, which effects in a temporary negative feedback (i.e., the oceanic CO_2 uptake kinetics cannot keep pace with rising CO_2 emissions). Nevertheless, these feedback evaluations are based on global assessments of the ocean and terrestrial reservoirs' ability in storing carbon in relation to changes in global atmospheric CO_2 concentration and climate. Therefore, the regional effect of carbon cycling on climate variability and their controlling mechanisms remain poorly understood. In this study, we further analyze the processes controling the strength climate-carbon cycle feedbacks in different regions.

Over land, climate change mostly impacts the tropical and northern high latitude regions. While an increase in ambient CO_2 concentrations stimulates net primary production and increases carbon storage in plant tissues, the consequences of warming generally lead to an increase in terrestrial soil respiration, thus induce carbon outgassing. The tropical regions respond most strongly to changes in the atmospheric CO_2 concentrations because plant assimilation of CO_2 is more efficient under warmer conditions. Higher soil respiration rates due to warming lead to a decline in soil carbon turnover time, predominantly at high latitudes where the change in surface temperatures is at a maximum.

In this study, the dynamical vegetation schemes improve the climate-carbon cycle feedback estimation since it allows the PFT to respond to warmer climate. Nevertheless, a more realistic estimation of the terrestrial biosphere feedback requires the inclusion of land-use changes, whose impact is expected to be in the same order of magnitude as that of the vegetation regime shifts.

Unlike for the terrestrial carbon cycle, there is no significant change in the global carbon uptake by the ocean between the similations with and without the effect of climate change. However, the fact that the atmospheric CO_2 concentration in the coupled simulation ends up higher than that in the uncoupled simulation suggests that there is a positive feedback mechanism between the climate and the ocean carbon cycle. Regional analysis indicates that different processes in different part of the world ocean contribute to dampen the relatively small carbon uptake changes between the two simulations. In addition, the consequences of climate change on ocean carbon uptake are not clearly apparent until the second half of this century.

Our study shows that there are both direct and indirect effects of climate change in altering oceanic carbon uptake. The direct effect include an increase in SST, which directly decreases the CO_2 gas solubility in seawater, most pronounced in high latitude regions. While increase in SST could also lead to reduced Revelle factor, our analysis shows that the simulated changes in Revelle factor is mostly dominated by changes in surface pCO_2, rather than SST. Additionally, changes in atmospheric circulation (i.e.,

surface wind stress) tend to increase the transfer rate of carbon between the air-sea interface, also most pronounced in high latitude regions. This effect would intensify carbon influx to the ocean in both carbon sink and carbon source regions. On average, changes in solubility and gas transfer rate of CO_2 alone would tend to decrease and increase carbon uptake by the ocean, respectively.

The indirect effects of climate change include, but are not limited to, changes in ocean circulation dynamics, mixed layer depth, sea ice extent, and fresh water fluxes. These indirect climate change factors significantly affect the high latitude Southern Ocean region. The summer sea ice extent in Antarctica, as simulated by the model, reduced almost to zero due to warming. This opening of sea ice induces stronger CO_2 gas transfer and deeper mixed layers, which in turn increase the transfer of carbon from the atmosphere to the ocean as well as from the surface into larger depths. A similar response to indirect effect of climate change is also shown in the Arctic region, where the model simulates a reduction of ~30% in sea ice extent. Over most of the North Atlantic regions, warming leads to shallowing of mixed layer depths and a slowdown of the overturning circulation, which favors the reduction of the vertical transport of surface DIC into deeper layers.

Acknowledgements. The authors would like to thank Martin Miles for thoroughly review the manuscript. We are also very grateful to Pierre Friedlingstein and the C4MIP group for the support and access to the original C4MIP data (used in Fig. 3). This study at the University of Bergen and Bjerknes Centre for Climate Research is supported by the EU-FP6 integrated project CarboOcean (grant nr. 511176), the Research Council of Norway funded project Nor-Clim and CarboSeason (grant nr. 1805/530). This is publication no. XXXX from the Bjerknes Centre for Climate Research.

References

Assmann, K. M., Bentsen, M., Segschneider, J., and Heinze, C.: An isopycnic ocean carbon cycle model, Geosci. Model Dev. Discuss., submitted, 2009.

Aumont, O., Maier-Reimer, E., Blain, S., and Monfray, P.: An ecosystem model of the global ocean including Fe, Si, P colimitations, Global Biogeochem. Cy., 17, 1060, doi:10.1029/2001GB001745, 2003. 851

Bleck, R., Rooth, C., Hu, D., and Smith, L. T.: Salinity-driven thermocline transients in a wind- and thermohaline-forced Isopycnic Coordinate Model of the North Atlantic, J. Phys. Oceanogr., 22, 1486–1505, 1992. 849

Bossuet, C., Déqué, M., and Cariolle, D.: Impact of a simple parameterization of convective gravity-wave drag in a stratosphere-troposphere general circulation model and its sensitivity to vertical resolution, Ann. Geophys., 16, 238–249, 1998, http://www.ann-geophys.net/16/238/1998/. 848

Cox, P. M., Betts, R. A., Jones, C. D., Spall, S. A., and Totterdell, I. J.: Acceleration of global warming due to carbon-cycle feedback in a coupled climate model, Nature, 408, 184–188, 2000. 869

Cramer, W., Bondeau, A., Woodward, F. I., Prentice, I. C., Betts, R. A., Brovkin, V., Cox, P. M., Fisher, V., Foley, J. A., Friend, A. D., Kucharik, C., Lomas, M. R., Ramankutty, N., Sitch, S., Smith, B., White, A., and Young-Molling, C.: Global response of terrestrial ecosystem structure and function to CO_2 and climate change: results from six dynamic global vegetation models, Glob. Change Biol., 7, 357–373, 2001. 856, 862

Crueger, T., Roeckner, E., Raddatz, T., Schnur, R., and Wetzel, P.:Ocean dynamics determine the response of oceanic CO_2 uptake to climate change, Clim. Dynam., 31, 151–168, doi:10.1007/s00382-007-0342-x, 2008. 865, 866

de Szoeke, R. A.: Equation of motion using thermodynamic coordinates, J. Phys. Oceanogr., 29, 2719–2729, 2000. 849

Déqué, M., Dreveton, C., Braun, A., and Cariolle, D.: The ARPEGE/IFS atmosphere model: A contribution to the French community climate modelling, Clim. Dynam., 12, 37–52, 1994. 848

Douville, H., Royer, J. F., and Mahfouf, J. F.: A new snow parameterization for the Météo-France climate model, Part II: Validation in a 3D GCM experiment, Clim. Dynam., 12, 37–52, 1995. 848

Drange, H. and Simonsen, K.: Formulation of air–sea fluxes in the ESOP2 version of MICOM, Technical Report 125, Nansen Environmental and Remote Sensing Center, Bergen, Norway, 23 pp., 1996. 850

Dukowicz, J. K. and Baumgardner, J. R.: Incremental remapping as a transport/advection al-

gorithm, J. Comput. Phys., 160, 318–335, 2000. 849
Farquhar, G. D., vo Caemmerer, S., and Berry, J. A.: A biochemical model of photosynthetic CO_2 assimilation in leaves of C_3 species, Planta, 149, 78–90, 1980. 861
Friedlingstein, P., Cox, P., Betts, R., Bopp, L., et al.: Climate-carbon cycle feedback analysis: Results from the C^4MIP model intercomparison, J. Climate, 19, 3337–3353, 2006. 847, 855, 857, 858, 860, 869, 879
Furevik, T., Bentsen, M., Drange, H., Kindem, I. K. T., Kvamst, N. G., and Sorteberg, A.: Description and evaluation of the bergen climate model: ARPEGE coupled with MICOM, Clim. Dynam., 21, 27–51, doi:10.1007/s00382-003-0317-5, 2003. 847, 848
Harder. M.: Dynamik, Rauhigkeit und Alter des Meereises in der Arktis, PhD. thesis, Alfred-Wegener-Institut für Polar-und Meeresforschung, Bremehaven, Germany, 124 pp., 1996. 850
Heimann, M. and Reichstein, M.: Terrestrial ecosystem carbon dynamics and climate feedbacks, Nature, 451, 289–292, doi:10.1038/nature06591, 2008. 847
Hickler, T., Smith, B., Prentice, I. C., Mjöfors, K., Miller, P., Arneth, A., and Sykes, M. T.: CO_2 fertilization in temperate FACE experiments not representative of boreal and tropical forests, Glob. Change Biol., 14, 1531–1542, doi: 10.1111/j.1365-2486.2008.01598.x, 2008. 861
Houghton, R. A. and Hackler, J. L.: Carbon flux to the atmosphere from land-use changes. Trends: A compendium of data on global change, Carbon Dioxide Information Analysis Center, US Department of Energy, Oak Ridge, TN, USA, 2002. 854
Hsu, Y. J. and Arakawa, A.: Numerical modeling of the atmosphere with an isentropic vertical coordinate, Mon. Weather Rev., 118, 1933–1959, 1990. 849
Janic, Z. I.: Pressure gradient force and advection scheme used for forecasting with steps and small scale topography, Beitr. Phys. Atmos., 50, 186–199, 1977. 849
Kucharik, C. J., Foley, J. A., Delire, C., Fisher, V. A., Coe, M. T., Lenters, J. D., Young-Molling, C., Ramankutty, N., Norman, J. N., and Gower, S. T.: Testing the performance of a dynamic global ecosystem model: water balance, carbon balance, and vegetation structure, Global Biogeochem. Cy., 14, 795–825, 2000. 856
Lott, F.: Alleviation of stationary biases in a GCM through a mountain drag parameterization scheme and a simple representation of mountain lift forces, Mon. Weather Rev., 125, 788–801, 1999. 848
Luo, Y.: Terrestrial carbon-cycle feedback to climate warming, Annu. Rev. Ecol. Evol. S., 38, 683–712, doi:10.1146/annurev.ecosys.38.091206.095808, 2007. 859

Maier-Reimer, E.: Geochemical cycles in an ocean general circulation model. Preindustrial tracer distribution, Global Biogeochem. Cy., 7, 645–677, 1993. 851
Maier-Reimer, E. and Hasselmann, K.: Transport and storage of CO_2 in the ocean-an inorganic ocean-circulation carbon cycle model, Clim. Dynam., 2, 63–90, 1987. 851
Maier-Reimer, E., Kriest, I., Segschneuder, J., and Wetzel, P.: The HAMburg Ocean Carbon Cycle Model HAMOCC5.1 - Technical Description Release 1.1, Berichte zur Erdsystemforschung 14, ISSN 1614-1199, Max Planck Institute for Meteorology, Hamburg, Germany, 50 pp., 2005. 851
Marland, G., Boden, T. A., and Andres, R. J.: Global, regional, and national CO_2 emissions. Trends: A compendium of data on global change, Carbon Dioxide Information Analysis Center, US Department of Energy, Oak Ridge, TN, USA, 2005. 854
McDougall, T. J. and Dewar, W. K.: Vertical mixing and cabbeling in layered models, J. Phys. Oceanogr., 28, 1458–1480, 1998. 850
McDougall, T. J. and Jackett, D. R.: An assessment of orthobaric density in the global ocean, J. Phys. Oceanogr., 35, 2054–2075, 2005. 849
Mikolajewicz, U., Groger, M., Maier-Reimer, E., Schurgers, G., Vizcaíno, M., and Winguth, A. M. E.: Long-term effects of anthropogenic CO_2 emissions simulated with a complex earth system model, Clim. Dynam., 28, 599–631, 2007. 866, 869
Otterá, O. H, Bentsen, M., Bethke, I., and Kvamstø, N. G.: Simulated pre-industrial climate in Bergen Climate model (version 2): Model description and large-scale circulation features, Geosci. Model Dev. Discuss., 2, 507–549, 2009. 851
Randall, D. A., Wood, R. A., Bony, S., Colman, R., et al.: Climate models and their evaluation, in: Climate Change, edited by: Solomon, S., Qin, D., Manning, M., Chen, Z., Marquis, M., Averyt, K. B., Tignor, M., and Miller, H. L., Cambridge University Press, Cambridge, United Kingdom and New York, 589–662, 2007. 847
Sabine, C. L., Feely, R. A., Gruber, N., Key, R. M., Lee, K., Bullister, J. L., Wanninkhof, R., Wong, C. S., Wallace, D. W. R., Tilbrook, B., Millero, F. J., Peng, T.-H., Kozyr, A., Ono, T., and Rios, A. F.: The oceanic sink for anthropogenic CO_2, Science, 305, 367–371, 2004. 856, 857, 868, 878
Salas-Melia, D: A global coupled sea ice-ocean model, Ocean Model., 4, 137–172, 2002. 851
Schmittner, A., Latif, M., and Schneider, B.: Model projections of the North Atlantic thermohaline circulation for the 21st century assessed by observations, Geophys. Res. Lett., 32, L23710, doi:10.1029/2005GL024368, 2005. 859

Sitch, S., Huntingford, C., Gedney, N., Levy, P. E., Lomass, M., Piao, S. L., Betts, R., Ciais, P., Cox, P., Friedlingstein, P., Jones, C. D., Prentice, I. C., and Woodwards, F. I.: Evaluation of the terrestrial carbon cycle future plant geography and climate-carbon cycle feedbacks using five Dynamic Global Vegetation Models (DGVMs), Glob. Change Biol., 14, 2015–2039, 2008. 860

Sitch, S., Smith, B., Prentice, I. C., Arneth, A., Bondeau, A., Cramer, W., Kaplan, J. O., Levis, S., Lucht, W., Sykes, M. T., Thonicke, K., and Venevsky, S.: Evaluation of ecosystem dynamics, plant geography and terrestrial carbon cycling in the LPJ dynamic global vegetation model, Glob. Change Biol., 9, 161–185, 2003. 852, 856

Six, K. and Maier-Reimer, E.: Effects of plankton dynamics on seasonal carbon fluxes in an ocean general circulation model, Global Biogeochem. Cy., 10, 559–583, 1996. 851

Takahashi, T., Sutherland, S. C., Wanninkhof, R., Sweeney, C., Feely, R. A., Chipman, D. W., Hales, B., Friedrich, G., Chavez, F., Sabine, C., Watson, A., Bakker, D. C. E., Schuster, U., Metzl, N., Yoshikawa-Inoue, H., Ishii, M., Midorikawa, T., Nojiri, Y., Kōrtzinger, A., Steinhoff, T., Hoppema, M., Olafsson, J., Arnarson, T. S., Tilbrook, B., Johannessen, T., Olsen, A., Bellerby, R., Wong, C. S., Delille, B., Bates, N. R., and de Baar, H. J. W.: Climatological mean and decadal change in surface ocean pCO_2, and net sea-air CO_2 flux over the global oceans, Deep-Sea Res. II, in press, 2009. 856

Taylor, K. E.: Summarizing multiple aspects of model performance in a single diagram, J. Geophys. Res., 106, 7183–7192, 2001. 855

Terray, L., Thual, O., Belamari, S., Déqué, M., Dandin, P., Lévy, C., and Delecluse, P.: Climatology and interannual variability simulated by the arpege-opa model, Clim. Dynam., 11, 487–505, 1995. 852

Tjiputra, J. F. and Winguth, A. M. E.: Sensitivity of sea-to-air CO_2 flux to ecosystem parameters from an adjoint model, Biogeosciences, 5, 615–630, 2008, http://www.biogeosciences.net/5/615/2008/. 867

Wanninkhof, R.: Relationship between wind speed and gas exchange over the ocean, J. Geophys. Res., 97, 7373–7382, 1992. 852, 865

Weiss, R. F.: The solubility of nitrogen, oxygen and argon in water and sea water, Deep-Sea Res., 17, 721–735, 1970. 852

Weiss, R. F.: Carbon dioxide in water and seawater: The solubility of a non-ideal gas, Mar. Chem., 2, 203–215, 1974. 852, 865, 866

Zeebe, R. E. and Wolf-Gladrow, D. E.: CO_2 in seawater: Equilibrium. Kinetics, Isotops, Elsevier

Oceanography Series, 65, 346 pp., Amsterdam, 2001. 868
Zickfeld, K., Eby, M., and Weaver, A. J.: Carbon-cycle feedbacks of changes in the Atlantic meridional overturning circulation under future atmospheric CO_2, Global Biogeochem. Cy., 22, GB3024, doi:10.1029/2007GB003118, 2008. 859

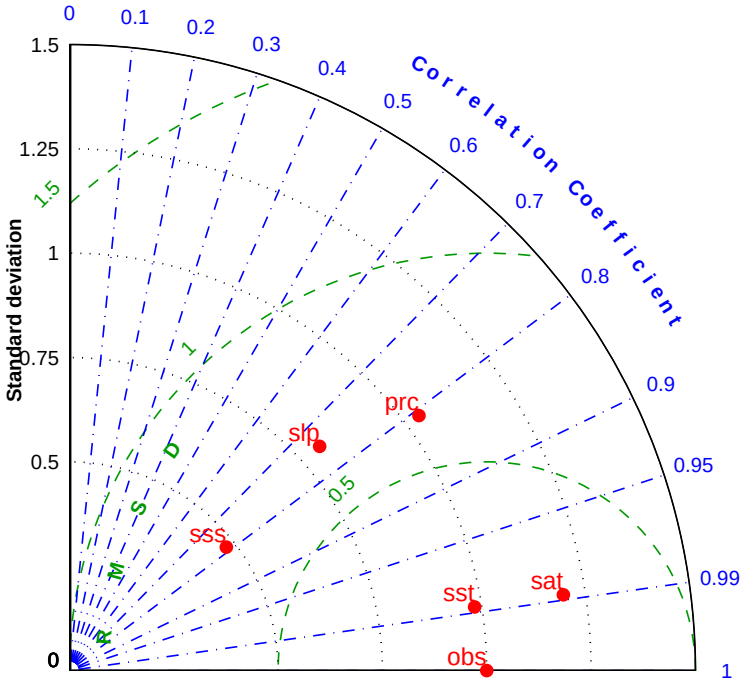

Fig. 1. Taylor diagram for annually-averaged sea surface temperature (sst), salinity (sss), surface air temperature (sat), precipitation (prc), and sea level pressure (slp) from the reference run (REF) (Possible also to add results from REF2 together) as compared to climatology Levitus and NCEP reanalysis.

GMDD
2, 845–887, 2009

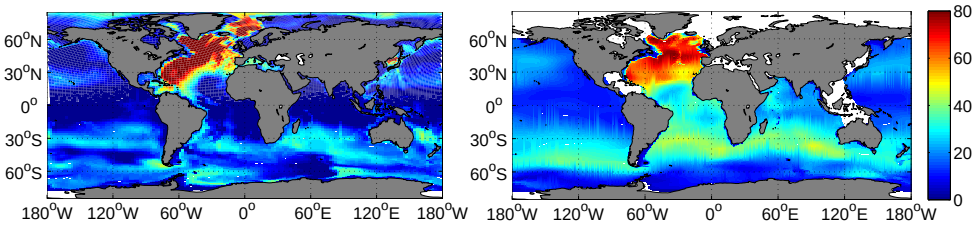

Fig. 2. Map of column integrated anthropogenic carbon content in the ocean for the year 1994 simulated by the BCM-C (left) and compared to the observation-based estimates (right) from Sabine et al. (2004). Units are in [mol C m^{-2}].

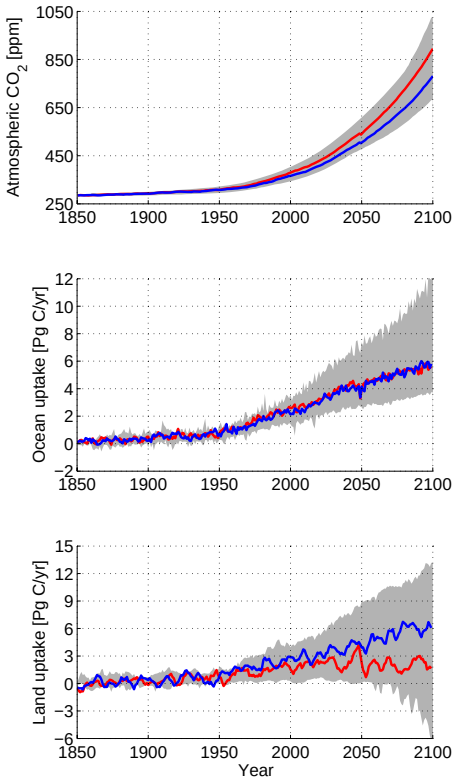

Fig. 3. BCM-C projection of annual (top) atmospheric CO_2 concentration, (middle) oceanic carbon uptake, and (bottom) terrestrial carbon uptake as compared to the range from other models (grey shading) (Friedlingstein et al., 2006). Red lines represent results from COU whereas blue lines represent results from UNC simulations.

GMDD
2, 845–887, 2009

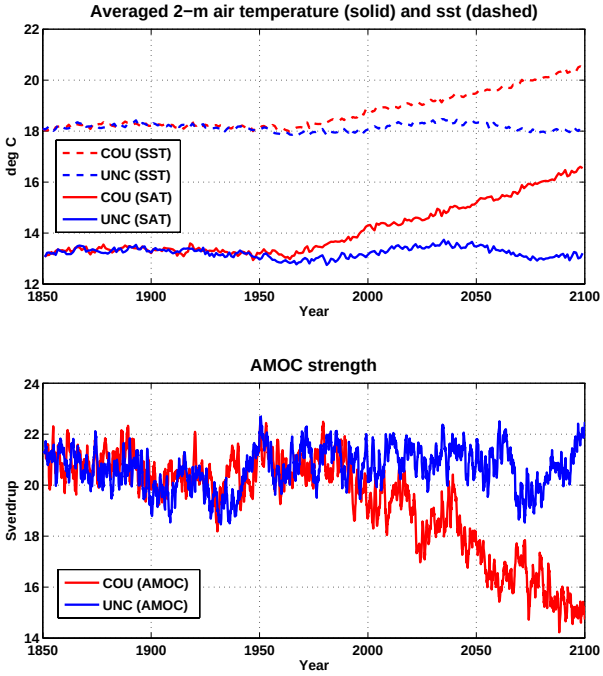

Fig. 4. Time-series of global mean (top) 2-m surface temperature and sea surface temperature and (bottom) strength of the Atlantic Meridional Overturning Circulation as projected by the BCM-C model for both the COU and UNC simulations. There is generally no significant trend changes in the UNC simulation because the changes in atmospheric CO_2 concentration has no radiative effect.

GMDD
2, 845–887, 2009

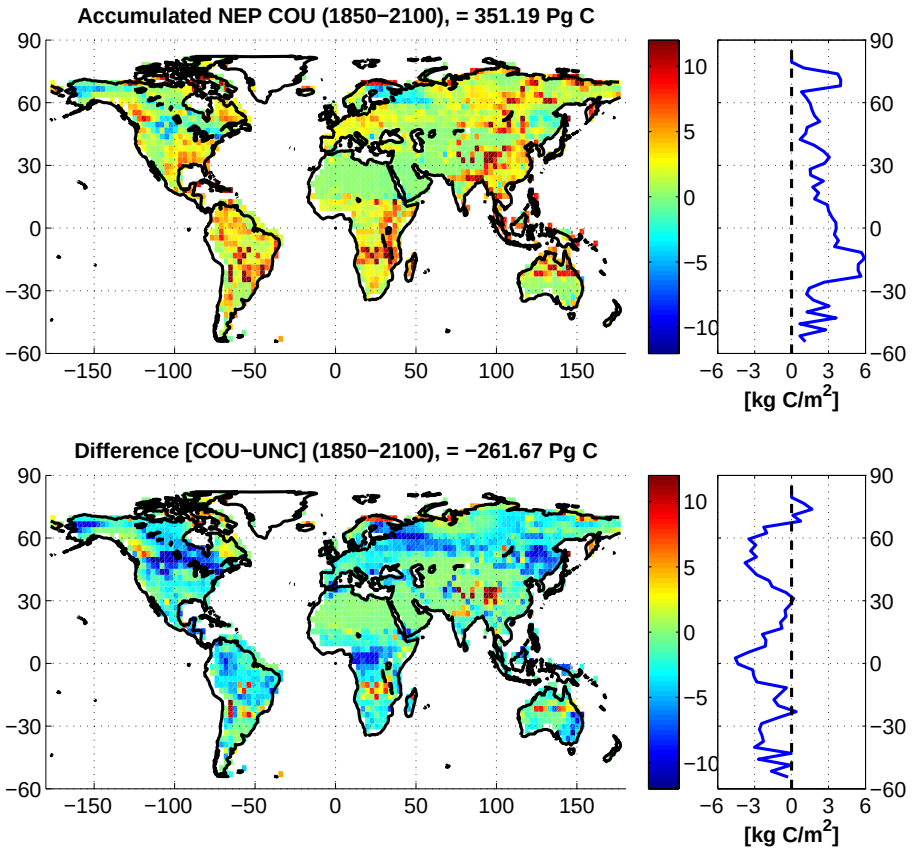

Fig. 5. Geograpical distribution of accumulated carbon uptake by the land [Pg C] (top) simulated by the COU simulation and (bottom) the difference between COU and UNC simulations. Right panel shows the latitudinal average of carbon uptake [Kg C/m^2].

GMDD
2, 845–887, 2009

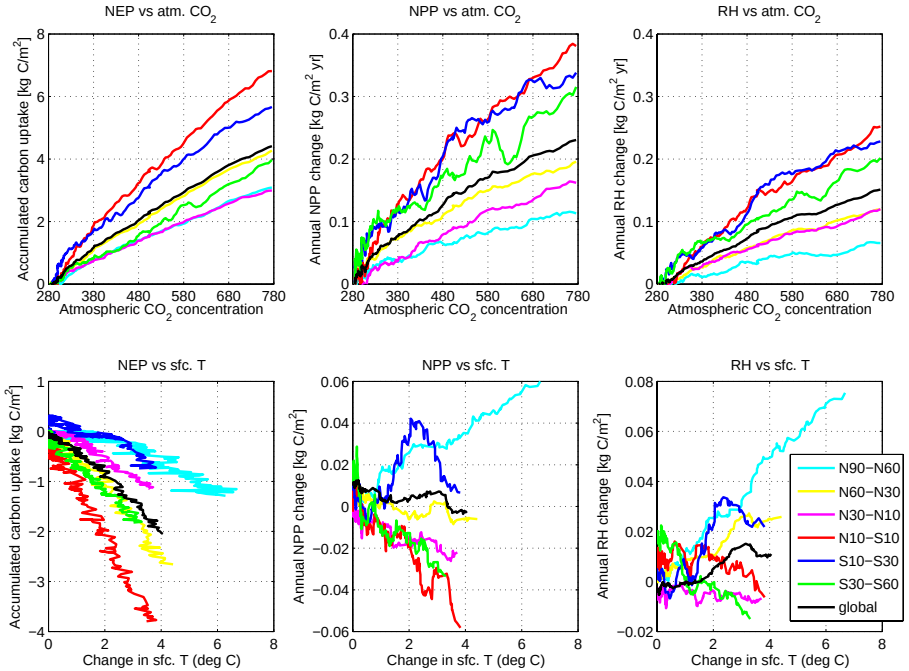

Fig. 6. (top-left) Latitudinal variability of terrestrial accumulated carbon plotted as a function of atmospheric CO_2 concentration. (top-center) Latitudinal sensitivity of annual land NPP change to changes in atmospheric CO_2. (top-right) Latitudinal sensitivity of heterotrophic respiration to changes in atmospheric CO_2. Bottom figures shows similar sensitivities to changes in surface temperature.

GMDD
2, 845–887, 2009

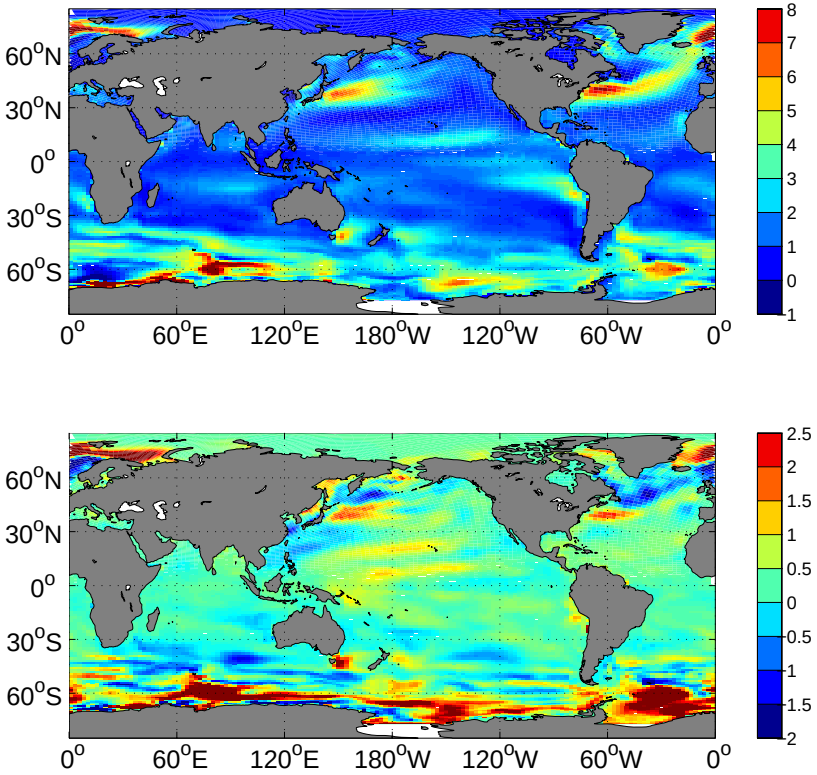

Fig. 7. Map of (top) time-integrated (1860–2099) changes in carbon uptake relative to the preindustrial period (1850–1859) from the COU simulations and (bottom) the difference between the fully coupled and the uncloupled simulations (COU-UNC). Units are in [kg C/m^2].

GMDD
2, 845–887, 2009

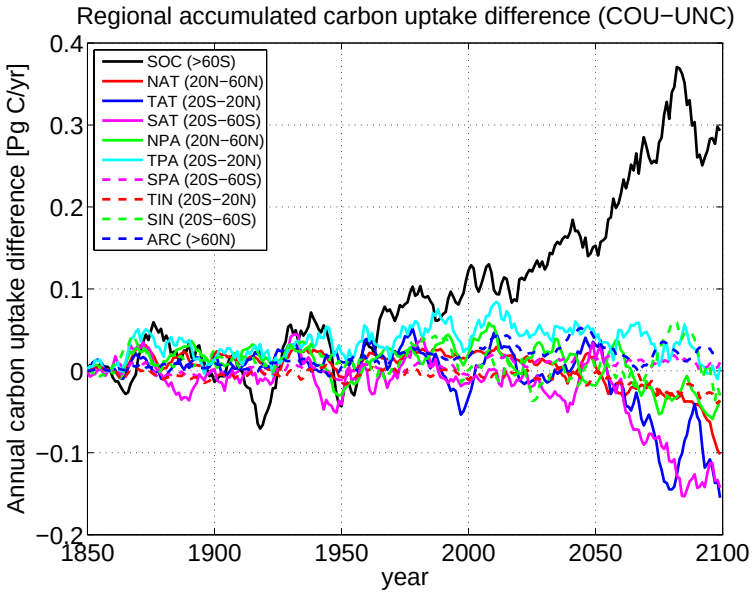

Fig. 8. Coupled minus uncoupled simulation of spatially integrated annual air-to-sea carbon flux (10-year running mean). Regions are defined as follow: Southern Ocean (SOC), North Atlantic (NAT), Tropical Atlantic (TAT), South Atlantic (SAT), North Pacific (NPA), Tropical Pacific (TPA), South Pacific (SPA), Tropical Indian (TIN), South Indian (SIN), and Arctic (ARC).

GMDD
2, 845–887, 2009

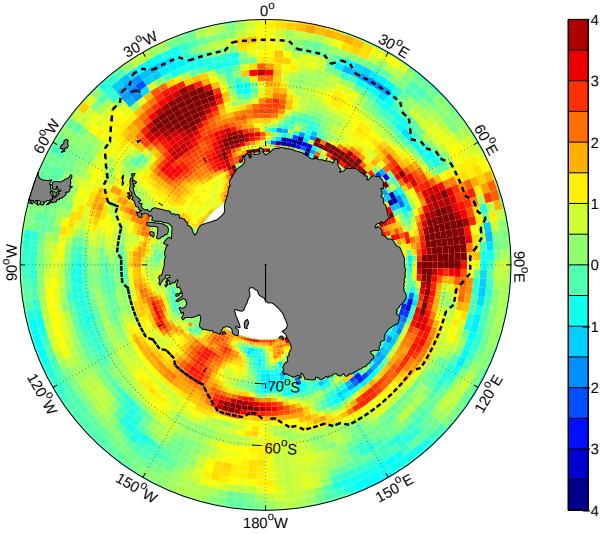

Fig. 9. Changes in atmospheric carbon uptake (Similar to Fig. 7b) for the Southern Ocean together with average winter (January, 2070–2099) sea-ice extent for the (solid black line) COU and (dashed black line) UNC simulations. Unit of color shades are in [kg C/m^2]

GMDD
2, 845–887, 2009

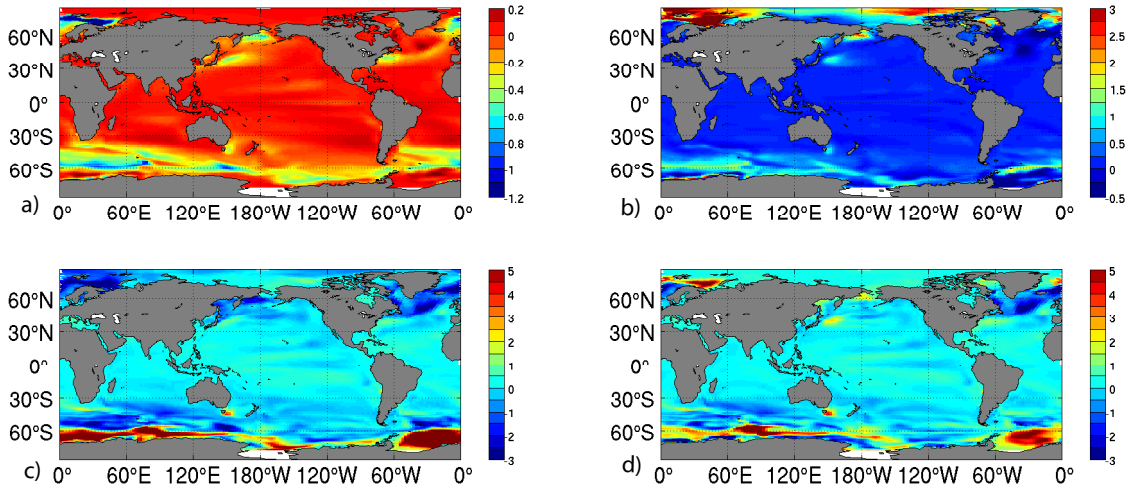

Fig. 10. Average changes in carbon uptake between the COU and UNC (2080–2099) due to the effects of the changes in **(a)** solubility, **(b)** gas transfer velocity, **(c)** difference in partial pressure of CO_2, and **(d)** actual simulated carbon uptake difference. Units are in [moles C m^{-2} yr^{-1}].

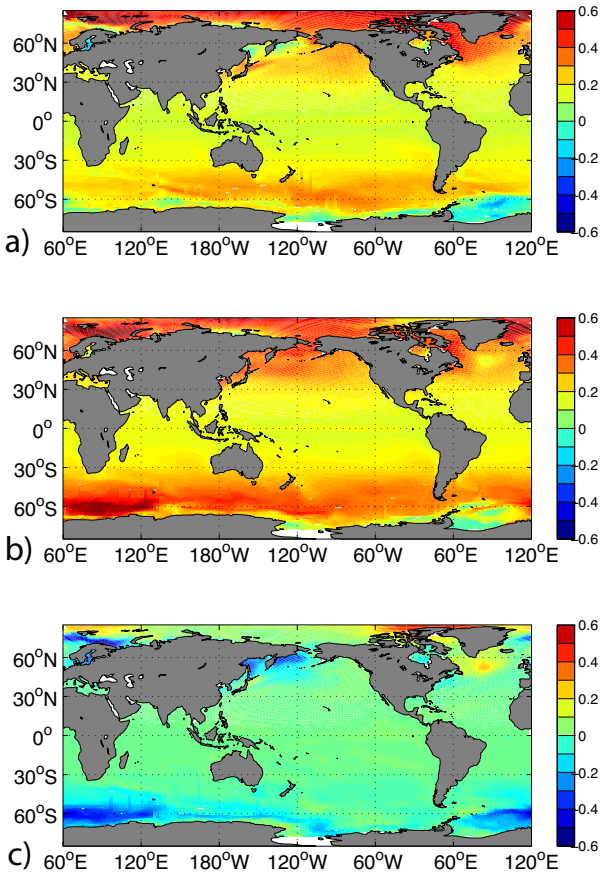

Fig. 11. Difference in Revelle factors between year 2099 and 1850 simulated in the **(a)** COU and **(b)** UNC simulations and **(c)** COU minus UNC for year 2099.

GMDD
2, 845–887, 2009